JGR Solid Earth

RESEARCH ARTICLE
10.1029/2022JB024390

The Influence of Grain Size Distribution on Laboratory-Generated Volcanic Lightning

C. Springsklee[1], B. Scheu[1], M. Manga[1,2], V. Cigala[1], C. Cimarelli[1], and D. B. Dingwell[1]

[1]Ludwig-Maximilians-Universität München, Munich, Germany, [2]University of California, Berkeley, Berkeley, CA, USA

Key Points:

- Electrical discharges are generated in experimentally decompressed volcanic ash
- The presence of fines (<10 μm), a broad grain size distribution, and dense particles promote laboratory-generated volcanic lightning
- The coupling of the particles to the jet determines whether an electrical discharge occurs within the jet

Supporting Information:

Supporting Information may be found in the online version of this article.

Correspondence to:

C. Springsklee and B. Scheu,
christina.springsklee@min.uni-muenchen.de;
b.scheu@lmu.de

Citation:

Springsklee, C., Scheu, B., Manga, M., Cigala, V., Cimarelli, C., & Dingwell, D. B. (2022). The influence of grain size distribution on laboratory-generated volcanic lightning. *Journal of Geophysical Research: Solid Earth*, *127*, e2022JB024390. https://doi.org/10.1029/2022JB024390

Received 15 MAR 2022
Accepted 19 SEP 2022

Author Contributions:

Conceptualization: C. Springsklee
Formal analysis: M. Manga, V. Cigala
Funding acquisition: B. Scheu, D. B. Dingwell
Investigation: B. Scheu
Methodology: C. Springsklee, B. Scheu, C. Cimarelli
Project Administration: B. Scheu
Resources: B. Scheu
Software: C. Cimarelli
Supervision: B. Scheu, M. Manga
Visualization: C. Springsklee

Abstract Over the last decades, remote observation tools and models have been developed to improve the forecasting of ash-rich volcanic plumes. One challenge in these forecasts is knowing the properties at the vent, including the mass eruption rate and grain size distribution (GSD). Volcanic lightning is a common feature of explosive eruptions with high mass eruption rates of fine particles. The GSD is expected to play a major role in generating lightning in the gas thrust region via triboelectrification. Here, we experimentally investigate the electrical discharges of volcanic ash as a function of varying GSD. We employ two natural materials, a phonolitic pumice and a tholeiitic basalt (TB), and one synthetic material (soda-lime glass beads [GB]). For each of the three materials, coarse and fine grain size fractions with known GSDs are mixed, and the particle mixture is subjected to rapid decompression. The experiments are observed using a high-speed camera to track particle-gas dispersion dynamics during the experiments. A Faraday cage is used to count the number and measure the magnitude of electrical discharge events. Although quite different in chemical composition, TB and GB show similar vent dynamics and lightning properties. The phonolitic pumice displays significantly different ejection dynamics and a significant reduction in lightning generation. We conclude that particle-gas coupling during an eruption, which in turn depends on the GSD and bulk density, plays a major role in defining the generation of lightning. The presence of fines, a broad GSD, and dense particles all promote lightning.

Plain Language Summary Explosive volcanic eruptions are accompanied by volcanic lightning (VL), which are electrical discharges resulting from particles that become electrically charged during eruption. We investigated experimentally the discharge behavior of three different materials by performing shock-tube experiments. We used different rocks and analog material. We focused on the abundance of particle sizes smaller <10 μm (very fine ash) by testing individual grain size fractions mixed with coarser grains. The jet behavior was recorded by a high-speed camera. We find that the presence of very fine particles has a major influence on the probability to produce electrical discharges within the particle-laden jet. Based on our experiments, more VL is expected when (a) fine ash is abundant, (b) there is a wide grain size distribution, and (c) the particles are dense.

1. Introduction

Explosive volcanic eruptions deliver volcanic ash (<2 mm) to the atmosphere. Ash grain size has a large effect on the residence time and dispersal of ash in the atmosphere (Ayris & Delmelle, 2012), and thereby influences the distribution and duration of impacts on the Earth System. Ash electrification and associated volcanic lightning (VL) are common phenomena accompanying explosive volcanism. They create opportunities to monitor and characterize vent properties in real time (Cimarelli & Genareau, 2022). Spectacular recent examples include the eruptions of Eyjafjallajökull in 2010 (Bennett et al., 2010), Calbuco in 2015 (Van Eaton et al., 2016), ongoing Sakurajima eruptions (e.g., Aizawa et al., 2016; Cimarelli et al., 2016; Vossen et al., 2021), Bogoslof in 2016–2017 (Van Eaton et al., 2020), Anak Krakatau in 2018 (Prata et al., 2020), Stromboli in 2019 (Vossen et al., 2022), and Hunga Tonga-Hunga Ha'apai in 2022 (Yuen et al., 2022).

Following the classification of Thomas et al. (2010), VL can be broadly subdivided into plume lightning, near-vent lightning, and vent discharges (Aizawa et al., 2016; Behnke et al., 2013, 2018; Cimarelli et al., 2016), each of which may be generated by a different combination of electrification mechanisms. Several studies have investigated the mechanisms that contribute to the build up of electrical charge and to charge separation in the volcanic plume: both processes that are required for the generation of electrical discharges (Arason et al., 2011; Björnsson et al., 1967; Cimarelli et al., 2014; James et al., 2000; Méndez Harper et al., 2021; Nicoll et al., 2019; Prata et al., 2020; Thomas et al., 2010; Van Eaton et al., 2020). The mechanisms include fracto-electrification due

Writing – original draft: C. Springsklee, B. Scheu, V. Cigala, C. Cimarelli, D. B. Dingwell
Writing – review & editing: C. Springsklee, M. Manga, V. Cigala, C. Cimarelli, D. B. Dingwell

to the fragmentation of magma and pyroclasts (James et al., 2000) and triboelectrification by frictional interaction of particles of different sizes (Cimarelli et al., 2014; Gaudin & Cimarelli, 2019; Méndez Harper et al., 2021).

Field observations, laboratory experiments, and numerical modeling have all been employed to investigate VL generation in different plume regions and to explore the parameters controlling the magnitude and frequency of VL. Investigations have focused on the influences of mass eruption rate (Hargie et al., 2019), plume height (Behnke et al., 2013; Bennett et al., 2010; Vossen et al., 2021), water content and temperature (Méndez Harper et al., 2020; Stern et al., 2019), and grain size distribution (GSD) (Gaudin & Cimarelli, 2019; Méndez Harper et al., 2021). In the context of the present study, the experiments performed by Gaudin and Cimarelli (2019) are particularly relevant. They concluded that the number of discharges is proportional to the amount of fine-grained particles <63 μm ("fines") in the sample, with an increase in the amount of fines in a bimodal GSD sample generating an increase in the number of discharges.

The common occurrence of VL is a clear demonstration of the fact that it is not restricted to a single composition of magma (McNutt & Williams, 2010). The chemical compositions of magmas vary over a wide range, which does however affect magma properties and their eruption styles and thus the probability of VL. In this study, three materials with different chemical compositions and bulk densities were tested under the same eruption conditions to isolate the effect of the particle size and composition on VL.

Méndez Harper and Dufek (2016) concluded that composition does not have a significant effect on charging behavior. In contrast, Forward et al. (2009b) investigated the triboelectric charging of granular synthetic materials, demonstrating differences in the triboelectric charging behavior for different materials. We also investigate explicitly the importance of fines by using different fractions of fines (particles <63 μm) to very fines (particles <10 μm). We evaluate how the GSD influences the electrical charging behavior with a focus on the very fine fraction and discuss the influence of chemical composition and bulk density on VL.

2. Experimental Procedure

2.1. Sample Preparation

We employed three materials: (a) soda-lime glass beads (GB), (b) tholeiitic basalt (TB), and (c) Laacher See phonolitic pumice (LSB). The materials differ in composition and texture and have been extensively characterized in previous studies (Cimarelli et al., 2011; Douillet et al., 2014; Gaudin & Cimarelli, 2019).

2.1.1. Soda-Lime Glass Beads (GB)

Soda-lime glass beads (GB) manufactured by the MHG Strahlanlagen GmbH consist of 70%–75% SiO_2, 12%–15% Na_2O, 7%–12% CaO, max. 5% MgO, max. 2.5% Al_2O_3, max. 1.5% K_2O, and max. 0.5% Fe_2O_3. The glass beads have a density of 2.45 g/cm^3. As this material lacks porosity, bulk density, and matrix density are equivalent. The grain size fractions used during the experiments were 150–250, 40–70, and <50 μm. The grain size fraction 40–70 μm was ground in a vibratory disc mill and sieved for 15 min to achieve fractions of 32–63, 25–32, <32, and <25 μm. To remove any finer particles adhering to the size fraction of interest, the size fractions of 32–63 and 25–32 μm were wet sieved under running distilled water and then dried in a furnace for ~12 hr at 90°C. An overview of the GSD of each fraction and a representative image of particles from each material are presented in Figure 1 and Table 1. A summary of the composition of the particle mixture that was used in each of the 96 experiments is given in more detail in the data set (Springsklee et al., 2022).

2.1.2. Laacher See Pumice (LSB)

The LSB particles come from the lower unit of the Laacher See eruption (East Eifel volcanic field, Germany). The LSB has been used in previous experiments (e.g., Gaudin & Cimarelli, 2019; Mueller et al., 2018; Stern et al., 2019) to simulate volcanic processes, including the generation of VL. The LSB is phonolitic in composition. The bulk density of the Laacher See pumice has been determined for different GSDs by Douillet et al. (2014) to be ~1.4 g/cm^3 for particles ranging in size from 0.125 to 16 mm. For particles in the range of 40–90 μm we determined a bulk density of 2.4 g/cm^3. This higher value corresponds to the matrix density of LSB, and the increase in bulk density likely results from these smaller size fractions being made from the melt surrounding larger bubbles. For the scaling to compare natural and experimental processes presented below, we adopt the value of 1.4 g/cm^3 as the coarse particles used in this experiment lie within the grain size range of 180–300 μm. The LSB

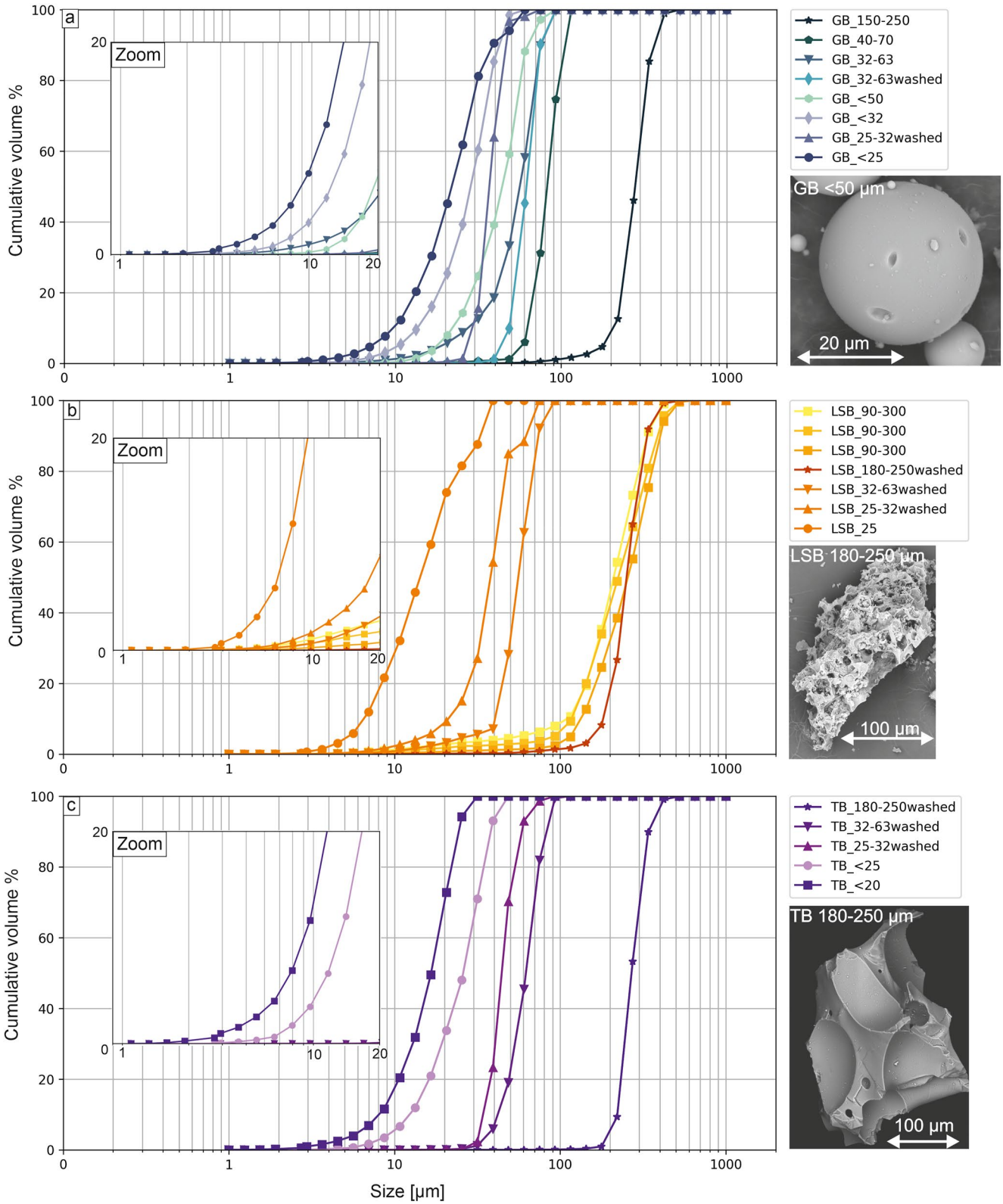

Figure 1. Grain size distribution of the sample fractions used in this study. (a) Overview of all fractions of soda-lime glass beads (GB) and an SEM image of a glass bead <50 µm in size; (b) overview of all fractions of Laacher See phonolitic pumice and an SEM image of a grain in the washed 180–250 µm fraction; (c) overview of all fractions of tholeiitic basalt and an SEM image of a particle in the 180–250 µm size fraction. A close-up of the size distribution of the very fine fractions is included as insets for all three materials.

Table 1
Summary of All Grain-Size Fractions Used in This Study

	Cumulative volume %							
Sample	10.0 µm	20.0 µm	25.0 µm	75.0 µm	100.0 µm	200.0 µm	300.0 µm	500.0 µm
GB_150-250	0.00	0.00	0.01	0.52	1.20	7.96	64.78	100.00
GB_40-70	0.00	0.18	0.37	31.19	89.59	100.00	100.00	100.00
GB_32-63	1.22	5.46	8.71	89.85	100.00	100.00	100.00	100.00
GB_32–63_washed	0.00	0.06	0.15	90.15	100.00	100.00	100.00	100.00
GB_<50	0.34	7.27	14.31	97.19	100.00	100.00	100.00	100.00
GB_<32	4.39	24.09	39.32	100.00	100.00	100.00	100.00	100.00
GB_25-32_washed	0.03	0.42	1.34	100.00	100.00	100.00	100.00	100.00
GB_<25	10.42	43.26	61.81	100.00	100.00	100.00	100.00	100.00
LSB_90-300_C41	1.30	2.79	3.25	6.34	8.53	45.33	81.24	99.94
LSB_90-300_C42.1	0.81	1.75	2.27	3.67	5.88	41.96	71.30	99.59
LSB_90-300_C42.2	0.31	0.74	0.95	1.70	2.83	31.96	63.43	99.31
LSB_180-250_washed	0.02	0.13	0.19	0.90	1.46	16.16	80.53	99.86
LSB_32-63_washed	0.85	3.19	4.63	92.20	100.00	100.00	100.00	100.00
LSB_25-32_washed	2.28	8.78	15.02	100.00	100.00	100.00	100.00	100.00
LSB_<25	28.42	72.72	81.54	100.00	100.00	100.00	100.00	100.00
TB_180250_washed	0.00	0.00	0.01	0.04	0.11	3.99	74.93	99.93
TB_32-63_washed	0.00	0.09	0.30	81.93	100.00	100.00	100.00	100.00
TB_25-32_washed	0.00	0.03	0.16	98.64	100.00	100.00	100.00	100.00
TB_<25	5.33	32.01	48.05	100.00	100.00	100.00	100.00	100.00
TB_<20	17.13	69.66	94.22	100.00	100.00	100.00	100.00	100.00

Note. For each sample, the grain size distribution (GSD) is given by the cumulative volume %. The samples were mixed to obtain the experimentally investigated GSD, comprising higher fractions of coarse versus fine particles.

was provided by ROTEC GmbH in an initial 90–300 µm bulk distribution. Four fractions were separated from the bulk sample. Three of them (90–300 µm) were used directly in experiments after determining their GSD. A fourth fraction was sieved to 180–250 µm and sieved under distilled water and dried. The remaining material was ground and sieved for 15 min to the grain size fractions of 32–63, 25–32, and <25 µm. The grain size fractions (180–250, 32–63, and 25–32 µm) were cleaned by sieving them under distilled water and dried in a furnace for ~12 hr at 90°C. For LSB, wet sieving had to be repeated to ensure sufficient removal of adhering "very fines" (<10 µm fraction). The grain size fraction 90–300 µm was used unmodified in the experiments, whereas the grain size fraction 180–250 µm was mixed in different proportions with the other finer grain size fractions for the experiments.

2.1.3. Tholeiitic Basalt (TB)

The tholeiitic basalt (TB) is from the 1975 to 1984 Krafla fires (Iceland) eruption. The coarse samples (180–250 µm) have an average bulk density of 2.87 g/cm^3. For particles <63 µm a density of 2.92 g/cm^3 was measured. In TB, we observed only a minor increase in density with decreasing grain size. TB samples are typically dense with very low porosity; therefore, bulk density is similar to the matrix density of 2.92 g/cm³, and only minor changes occur between grain sizes. The scaling was done with the density of the coarse grain size fraction (180–250 µm). TB, collected in 2019, showed surface organic contamination. Thus, we performed a thorough cleaning process. The first step was to clean the rocks with distilled water and dry overnight at 90°C. Next, the sample was immersed in H_2O_2 (10 vol%) for a week to remove organic matter. Finally, the rocks were again rinsed with distilled water and dried overnight at 90°C. To achieve the desired grain size fractions (180–250, 32–63, 25–32, <25, and <20 µm), the rocks were ground with a disc mill and sieved for 15 min. The grain size fractions (180–250, 32–63, and 25–32 µm) contained small amounts of a very fine fraction attached to the larger grain

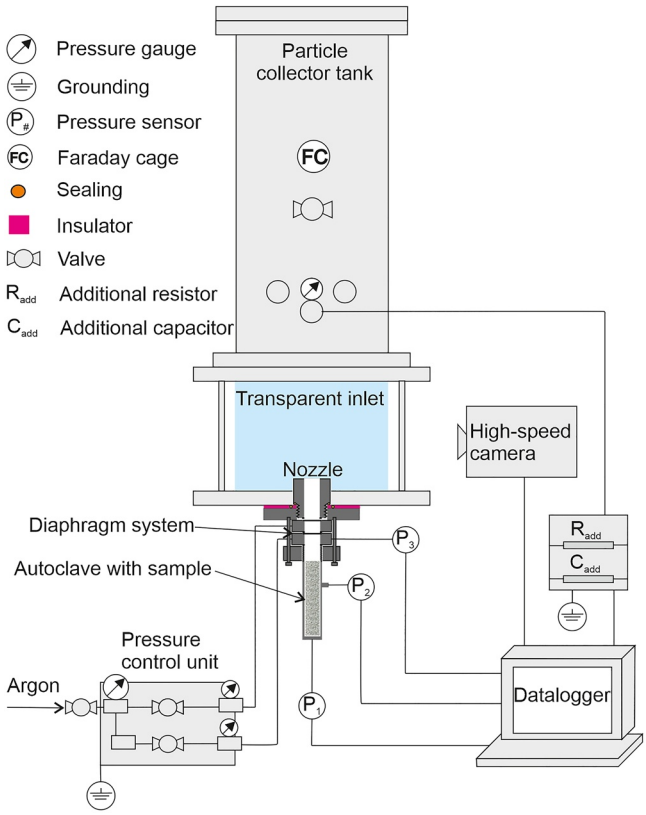

Figure 2. Experimental apparatus. The upper part, the particle collector tank, is insulated from the ground and the decompression system by a plastic flange (pink). It serves as a Faraday cage and discharges from the jet to the nozzle are recorded by the data logger. An additional resistor allows computing the electrical current (I) by measuring the voltage (V). The additional resistor decreases the amplitude of the signal and avoids saturation. The lower part of the particle collector tank is a transparent glass inlet, which enables the recording of the jet behavior during decompression with a high-speed camera.

surfaces (despite sieving). We therefore we cleaned those fractions by wet sieving to remove any adhering very fine fraction.

The grain size fractions of all three materials were analyzed using a Bettersizer S3 plus (3P Instruments GmbH & Co. KG) using two high-speed cameras (10x and 0.5x magnification). The grain size measurements by image analysis allows a combined size and shape analysis. A comparison between the circularity and the aspect ratio (length over diameter, L/D, and ratio) of the analyzed particles is given in Figures S1 and S2 in Supporting Information S1. The particles exhibit similar circularities as well as L/D ratios. All grain size fractions, which were sieved under distilled water, are hereafter referred to as "washed." For the TB and the LSB, the grain size fraction was 180–250 μm, and for the GB, the fraction 150–250 μm was mixed homogenously with varying weight percent of the smaller grain size fractions of the same material.

2.2. Experimental Apparatus

The experimental setup is a vertical shock-tube apparatus designed to perform rapid decompression experiments. Our apparatus is a modified version of the setup first described by Alidibirov and Dingwell (1996). Modifications have enabled the detection and quantification of experimental VL during rapid decompression of loose samples (Cimarelli et al., 2014; Gaudin & Cimarelli, 2019; Stern et al., 2019). In this study, a mobile gastight version of this apparatus was developed (Figure 2) where the upper part, the particle collector tank, serves as a Faraday cage (FC) to measure discharges.

We performed 96 experiments: 29 using LSB, 31 using TB, and 36 using GB. The experiments were carried out using an autoclave 26 mm in diameter and 160 mm in length. The particle mixture was inserted into the autoclave after weighing the sample (90 g for TB, 113 g for GB, and 30 g for LSB). The volume used was approximately kept the same for all samples, by keeping the initial sample weight constant for each material. The change in packing and GSD yielded differences in the filling height (f_h) of the autoclave (~130 mm for TB, ~148 mm for GB, ~132 mm for LSB 180–250 μm and ~115 mm LSB 90–300 μm). The average volume of all samples used in this study is 71.1 ± 6.4 cm^3. Compaction of the sample was carefully avoided by abstaining from shaking or knocking the autoclave. The filled autoclave was attached to the diaphragm system, and the sample was slowly pressurized by argon gas up to an average pressure of 10.37 ± 0.16 MPa (1 standard deviation). Autoclave pressure was monitored by a series of pressure sensors. The diaphragm system, which separates the pressurized sample from the low-pressure particle collector tank, consists of two scored diaphragms each with a burst pressure below the experimental target pressure. The controlled rupture of the diaphragms results in rapid decompression of the pressurized sample. The sample was ejected through the nozzle into the particle collector tank. The gastight particle collector tank is equipped with a pressure gauge that monitors tank pressure during the autoclave decompression.

The lower part of the particle collector tank is made of transparent glass and enables the recording of the ejection of the sample using a high-speed camera (Vision Research Phantom v711). We used the high-speed camera to monitor changes in the vent exit behavior of the expanding gas and gas plus particles mixture during the vertical expansion of the experimental jets. In particular, we monitored the expansion angle to identify the occurrence of a turbulent annulus of fine particles surrounding the collimated flow of larger particles in the core of each jet. The video recordings also captured some electrical discharge events but cannot be used to reliably quantify all discharges because some were obscured by particles in the jet.

The signal of the pressure sensors attached to the autoclave and the diaphragm system, the high-speed camera, and the FC connected to a data logger (Yokogawa WE7000) are synchronized and recorded simultaneously.

Once the flow has started, the interaction of the differently sized particles in the jet results in electrical charging, and charge separation will result in discharges. Discharges from the jet to the nozzle were detected and recorded by the data logger. Discharges within the jet were not recorded as they are not detected by the data logger.

We avoided any potential disturbances by particles reflected from the lid of the tank in the discharge signal by restricting our observations to the discharges within the first 5 ms of the experiments. Assuming that the gas and particle mixture traveled at the speed of sound in dry air, ~4.8 ms is the two-way travel time between the nozzle and the lid. Indeed, the analysis of the high-speed videos showed that after 4.4–4.8 ms, some very fine particles were moving downwards. The collector tank in all experiments was initially at ambient air pressure and room temperature. The conditions in the lab were kept constant at a temperature of 20.3°C ± 0.9°C and a relative humidity of 29.1 ± 8.6% RH. The decompression of the sample resulted in a pressure increase of ~0.2 MPa in the particle collector tank.

The detected charging decays approximately exponentially with time. We analyzed the raw signal (the measured electrical current) with a processing code developed by Gaudin and Cimarelli (2019) that deconvolves the instrument response from the raw data and counts the number of individual events and computes their magnitude. The capacitance of the setup was calculated as described in Gaudin and Cimarelli (2019). To evaluate the jet behavior after expansion, we used MTrackJ, an ImageJ plug-in, to determine the exit angle of the gas and particle mixtures at the vent during the experiments from the high-speed recordings. The gas opening angle was determined after the upper diaphragm opened and the jet was expanded, meaning it reached the top of the visible field of view, typically, five frames after the opening. Forty-one experiments were recorded with a frame rate of 14,217 frames per second (fps), and eight experiments were recorded with a frame rate of 50,000 fps. The particle opening angle was determined 20 frames after the first particles were visibly ejected through the nozzle when the frame rate was 14,217 fps and 70 frames after the first visible particles when the frame rate was 50,000 fps.

2.3. Scaling

In order to understand the physical processes that lead to the charging of particles and discharge in the jet, and to enable some comparison with volcanic eruptions, we use the following calculations and dimensionless numbers.

In order to compare measurements of the number and magnitude of discharge events between experiments with different materials and properties, we compare these measures with the energy density (ρE) multiplied by the percentage of very fine (<10 μm) particles. The energy E for an adiabatically expanding gas was calculated after Scheu and Dingwell (2022) as:

$$E = \frac{P_0 V_{\text{gas}}}{\gamma - 1}\left[1 - \left(\frac{P_{\text{atm}}}{P_0}\right)^{\frac{\gamma-1}{\gamma}}\right] \quad (1)$$

where P_0 is the applied overpressure, P_{atm} is the atmospheric pressure, V_{gas} is the volume of the gas within the autoclave, and γ is the adiabatic coefficient of argon at 10 MPa and 21°C ($\gamma = 1.99$).

The total volume of the gas (V_{gas}) is the difference between the volume filled with particles and the condensed volume (dense rock equivalent) of the particles, calculated based on their weight and density. The filling volume was calculated based on the filling height (f_h) and the radius (r) of the autoclave. The volume of the sample is the mass of the sample divided by its matrix density ρ_{m}:

$$V_{\text{gas}} = \pi r^2 f_h - \frac{m}{\rho_{\text{m}}}. \quad (2)$$

A volume normalization allows us to compare experimental results for samples of different sizes and is expressed as the energy density ρE:

$$\rho E = \frac{E}{V_{\text{sample}}} \quad (3)$$

where E is the energy and V_{sample} is the sample's total volume in the autoclave.

To compare natural processes and experiments, and to understand dynamics within the experiments, it is essential to compare the dynamics of the natural and experimental processes by a nondimensional analysis of the main controlling forces on the flow (e.g., Andrews & Manga, 2011, 2012; Burgisser et al., 2005; Cigala et al., 2017; Jessop & Jellinek, 2014; Roche, 2012; Roche & Carazzo, 2019; Weit et al., 2018, 2019). Here, following these previous studies, we determine the Reynolds number of the flow, the Froude number, and the Stokes number for a range of particle sizes and velocities to characterize the relevant processes we observe.

Following Weit et al. (2018), the Reynolds number Re of the biphasic mixture was calculated as:

$$\mathrm{Re} = \frac{2\rho_{\mathrm{mix}} U_{\mathrm{mix}} r}{\mu_{\mathrm{mix}}} \tag{4}$$

where subscripts mix refer to the properties of the gas + particle mixture. For similar experiments, but coarse GSD (i.e., from 0.5 to 2 mm particle diameter), Cigala et al. (2017) measured particle velocities up to 300 m/s, while Gaudin and Cimarelli (2019) with GSDs similar to our GSD estimated flow velocities between 200 and 500 m/s. Based on these results, the velocity U_{mix} was estimated to vary between 200 and 300 m/s. The characteristic length $2r$ in Equation 4 is the diameter of the nozzle. The density ρ_{mix} and viscosity μ_{mix} of the mixture were defined as:

$$\rho_{\mathrm{mix}} = C\rho_{\mathrm{s}} + (1 - C)\rho_{\mathrm{f}} \tag{5}$$

where C is the mean volume concentration, ρ_{s} is the bulk density of the sample, and ρ_{f} is the density of the transporting gas (Weit et al., 2018). The mean volume concentration C was calculated from:

$$C = \frac{\frac{m}{\rho_{\mathrm{s}}}}{U_{\mathrm{mix}} A\, t} \tag{6}$$

where A is the cross-sectional area of the autoclave. In this study, an experiment lasts over a time period of $t \sim 0.15$ s to eject almost all material, but this would lead to an underestimation of the concentration of the flow at the beginning of the experiment, which is the focus of this study. Because most of the material is ejected in the first 0.01 s and almost all discharges take place in this time range, the concentration was calculated with $t = 0.01$ s. Given these approximations, the concentration is slightly overestimated.

The viscosity of the mixture, μ_{mix}, was calculated (Weit et al., 2018) from:

$$\mu_{\mathrm{mix}} = \left(1 + \frac{5}{2} C\right) \mu_{\mathrm{f}} \tag{7}$$

where μ_{f} is the viscosity of the fluid.

The Froude number, which compares the inertia of the flow with the forces from gravity, was calculated (Andrews & Manga, 2011) from:

$$\mathrm{Fr} = \frac{U_{\mathrm{mix}}}{\sqrt{2g' r}} \tag{8}$$

where g' is the reduced gravity, calculated as:

$$g' = g\left(\frac{\rho_{\mathrm{mix}} - \rho_{\mathrm{f}}}{\rho_{\mathrm{mix}}}\right) \tag{9}$$

The Stokes number St describes how well particles are coupled to the time-varying flow. Since electrical discharge requires both collisions between particles and then separation of charged particles, the Stokes number is particularly important because it influences both collisions and subsequent particle motions. St was calculated as the ratio of the particle drag response time, τ_{p}, to the overturn time of an eddy, τ_{f}:

$$\mathrm{St} = \frac{\tau_{\mathrm{p}}}{\tau_{\mathrm{f}}} \tag{10}$$

The particle drag response time τ_p was calculated from:

$$\tau_p = \frac{(\rho_s - \rho_f)\, d^2}{18\mu_f} \tag{11}$$

where d is the particle diameter. The overturn time of an eddy τ_f was determined experimentally by Jessop and Jellinek (2014) as:

$$\tau_f = \frac{10 r_0}{U_{mix}} \tag{12}$$

where r_0 is the nozzle radius. The factor of 10 in Equation 12 and other approximations lead to uncertainties in our estimates of the various ratios of forces and time scales. However, these dimensionless parameters provide the order of magnitude of the dynamics and thus the relationship between our experiments and volcanic eruptions.

3. Results

3.1. Discharge Experiment

Figure 3 summarizes the electrical discharge measurements. The experiments with GB and a GSD of 150–250 and 40–70 μm showed no discharges. To test the impact of increasing polydispersity, one experiment with GB (EXP 168) including 10 wt% of particles 40–70 μm in size was performed and did not have any detected discharge. The next smaller grain size fraction tested for GB was 32–63 μm. One fraction of this grain size was washed, whereas another fraction was not. Experiment 227 was performed with 5 wt% of the washed grain size fraction 32–63 μm, and this GSD did not generate any discharges during the first 5 ms of ejection. The same mixture was prepared with the unwashed fraction 32–63 μm and was used in experiments 217 and 221. During experiments 217 and 221, there were 18 and 29 discharges detected, respectively. Experiments containing the washed grain size fraction 25–32 μm only led to small amounts of discharge. In the experiments that included the grain size fraction <25 μm, sample mixture is correlated with discharges (Figure 3). The variation in the proportion of the very fine fraction in the sample changes the total number and the total magnitude of discharges.

Similar behavior can be observed for the experiments conducted with the TB particles (Figures 3c and 3d). For this material, fewer GSDs were tested compared to the GB. However, also in this case, samples containing no particles <10 μm produced almost no discharges. The samples containing particles <25 μm with a significant fraction of very fines (<10 μm) were accompanied by discharges. Additionally, a sample containing a fraction <20 μm was prepared and tested, and a significant number of discharges were measured. These experiments show that increasing the fraction of very fine particles produces an increase in the number of electrical discharges (Figure 3). We observe an apparently asymptotic behavior of the number of discharges versus fine particle concentration (Figure 3d) that may indicate a charge saturation limit for which further increments of very fine particles in the mixture will cause no increase in the discharge number. The same asymptotic behavior is observed in the magnitude of discharge as a function of increasing fractions of very fine particles (Figures 3a and 3c).

LSB particles behave significantly differently compared with GB and TB (Figure 3). As for GB and TB, LSB does not show discharges for the sample with the added size fractions 32–63 and 25–32 μm. Yet, the charging behavior for LSB differs from GB and TB, as adding a fine grain size fraction of <25 μm does not generate significant discharge (Figure 3). Three unwashed samples with a GSD of 90–300 μm were tested for comparison. The grain size fractions 90–300 μm showed a significant amount of discharge and displayed a linear increase in the magnitude of discharge with increased very fines (<10 μm). The variability of the discharge measured in the experiment increased relative to GB, perhaps because of the higher variance in the GSD.

Comparing the three different materials, TB and GB particles both display an increase in total magnitude of discharge by increasing the number of very fines (<10 μm) (Figure 3). The total discharge magnitude of TB is slightly higher than that of the GB particles. For LSB, only the unwashed and broader grain size fraction 90–300 μm shows a similar behavior. However, the increase in total magnitude of discharge with increasing fraction of very fines is less pronounced and no asymptotic behavior could be observed (Figure 3).

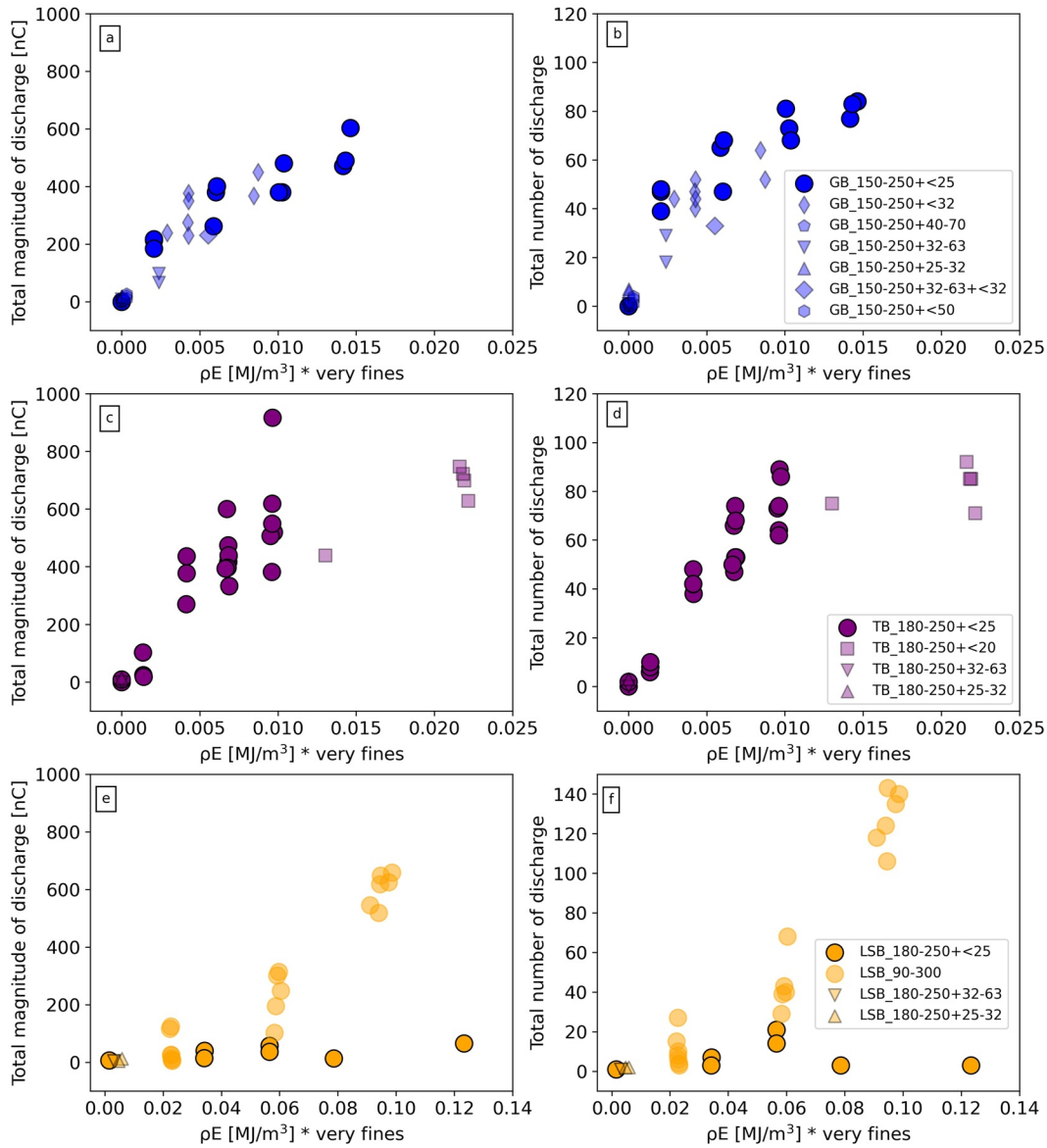

Figure 3. Measurements of volcanic lightning for tholeiitic basalt, soda-lime glass beads, and Laacher See phonolitic pumice. The total magnitude of discharge is displayed as a function of the energy density multiplied by the percentage of very fine fraction (<10 μm) in panels (a, c, and e) and the total number of discharges as a function of energy density multiplied by the percentage of very fines is displayed in panels (b, d, and f).

3.2. Vent Exit Behavior

High-speed video enables the determination of the exit angle of the experimental jet (Figure 4). The video recordings of the nine experiments are provided as Movies S1, S2, S3, S4, S5, S6, S7, S8, and S9. The vent exit angle of the gas-particle mixture α_{gp} was measured and compared to the vent exit angle of the preceding expanding particle-free gas α_g. The value of α_g is approximately constant for all experiments at a value of $28.6 \pm 1.9°$, that is, independent of the material or original GSD. We note that the applied pressure and temperature in all experiments were very similar, and the carrier gas is the same for all experiments.

The value of α_{gp} varies much more widely. The TB and GB particles exhibit similar trends in their vent exit behavior; that is, α_{gp} increases with increasing fraction of very fines (Figure 4). In order to capture the evolution of the vent exit behavior of the gas-particle mixture, we define a ratio Γ between the exit angles of gas-particle mixtures divided by the exit angle of the gas phase only: $\Gamma = \alpha_{gp}/\alpha_g$. A ratio $\Gamma < 1$ describes a narrowing of the

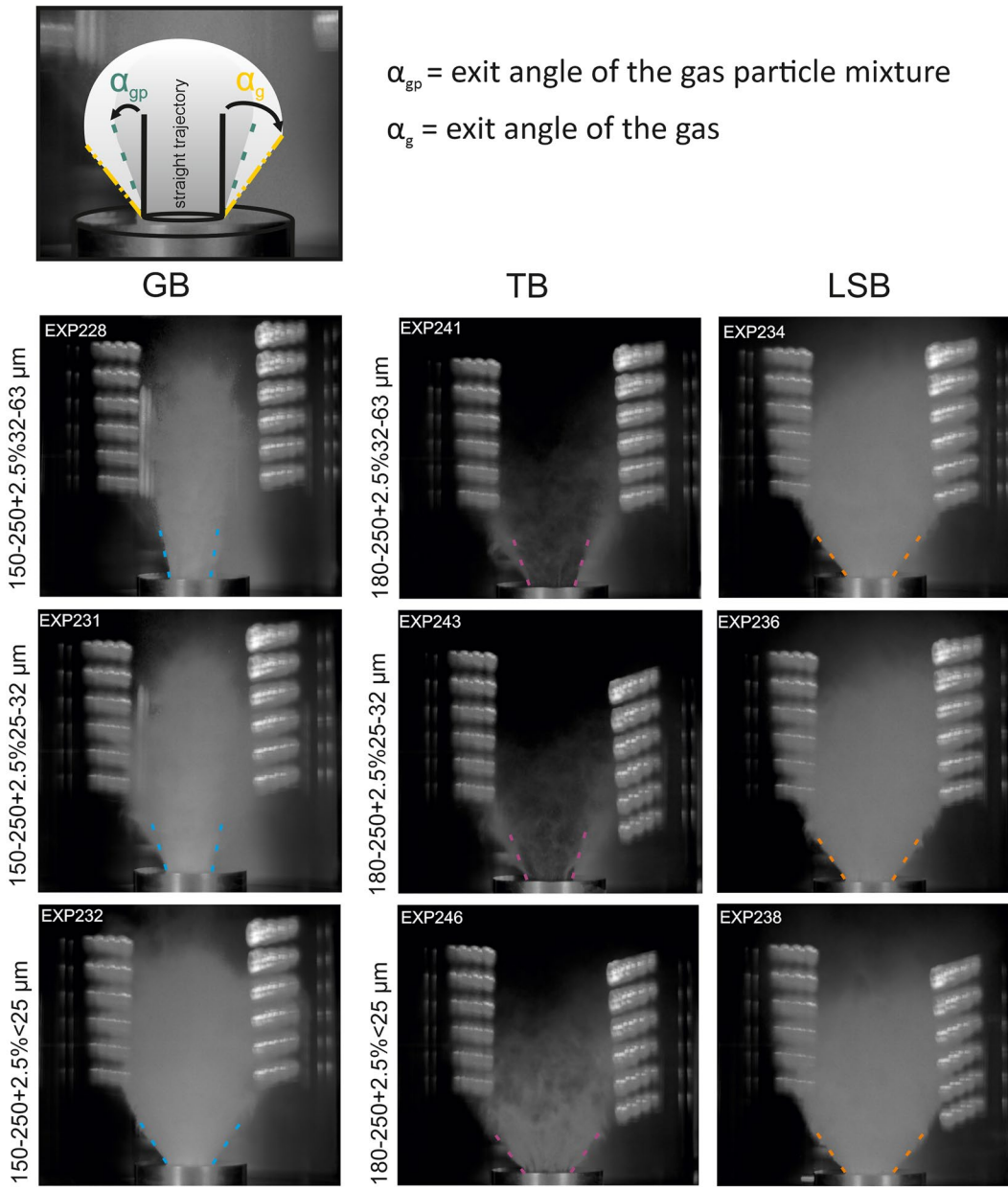

Figure 4. Illustrations of the vent exit behavior of the different materials after decompression. The schematic drawing in the upper left defines the exit angles. The exit angle of the gas-particle suspension was measured 20 frames (for a frame rate of 14,217 fps) or 70 frames (a frame rate of 50,000 fps) after the first particles were ejected through the nozzle. The exit angle of the gas-particle mixture (α_{gp}) is drawn in the images with the dashed colored lines.

jet exit angle, which is observed for no to very minor fractions of very fine particles. We speculate here that, for the case of a small number very fine fraction, (TB with 0.5 wt% of fines (ρE [MJ/m^3] * very fines = 0.0014), the fine particles form a mixed layer surrounding the collimated flow in the middle of the jet. As this mixed layer is likely highly diluted and thus cannot be identified in the high-speed video recordings (especially when the very fine fraction is low), it might lead to a bias in the measured α_{gp}. $\Gamma > 1$ describes an enhanced expansion of the jet (Figure 5). For GB and TB, we observe that Γ is most sensitive to small amounts of very fines and seems to become increasingly insensitive to the addition of further amounts of very fine particles once a value of ~1.3 is reached.

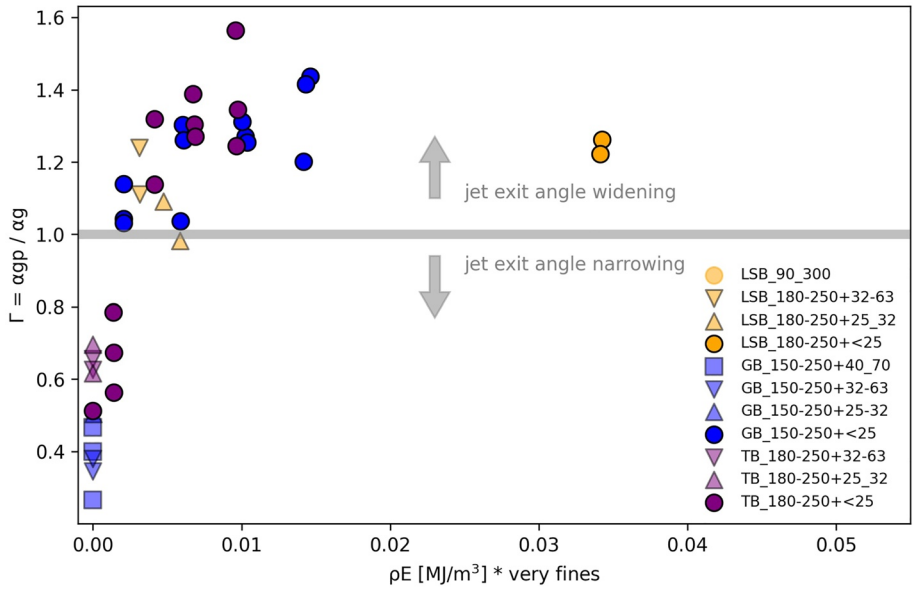

Figure 5. The vent exit behavior of the jet was characterized by the ratio of the vent exit angle of the gas-particle mixture and the vent exit angle of the gas ($\Gamma = \alpha_{gp}/\alpha_g$, where α_{gp} is the exit angle of the particle laden jet and α_g is the exit angle of the gas, as illustrated in Figure 4) as a function of the energy density multiplied by the percentage of very fines (<10 μm). A value for $\Gamma < 1$ indicates a narrowing of the jet, whereas a value for $\Gamma > 1$ indicates a widening. The gray line $\Gamma = 1$ indicates that the gas exit angle and the gas-particle mixture angle are equal.

This trend could not be confirmed or refuted for the LSB, because we could not completely quantitatively remove the very fine fraction. Here, values for α_{gp} and thus Γ are quite similar for all experiments. In addition, after decompression, the less dense LSB particles appear to be more coupled to the expanding gas phase than the denser TB and GB particles of the same size.

4. Discussion

Triboelectrification has been found to be the dominant charging process for near-vent discharges in shock-tube experiments (Gaudin & Cimarelli, 2019; Rayborn & Jellinek, 2022). Gaudin and Cimarelli (2019) also used LSB under similar applied pressure conditions as in this study and did not observe a significant grain size reduction in their experiments using a 4 m long particle collector tank. We can thus exclude primary sample fragmentation as a significant mechanism for electrification. Hereafter, triboelectrification will be considered the key mechanism in charging particles compared to fracto-electrification, though the contribution of other charging mechanisms cannot be fully excluded. Nondisruptive interaction or collision between particles produces charging where charge of opposite polarity is separated between large and fine particles (Forward et al., 2009a; Kikuchi & Endoh, 1982; Méndez Harper et al., 2021), and leads to a size-dependent bipolar charging mechanism.

The interaction of particles with each other depends on their coupling to the gas phase and whether the flow is turbulent. The Reynolds number Re_{mix}, the ratio of inertial to viscous forces within the fluid, for natural volcanic plumes usually ranges between 10^7 and 10^9 (see Table 2) and implies turbulent conditions ($Re > 10^4$). Burgisser et al. (2005) highlight the importance that experiments reach $Re > 10^4$ to investigate volcanic processes in jets, plumes, and pyroclastic density currents. In this study, a similarly high Reynolds number ($Re \sim 10^6$–10^7) is reached based on the high velocities achieved during the initial phase of decompression. The empirical principle called "Reynolds-number independence" states that provided Re is high enough, its exact value does not strongly influence the overall dynamics (Paola et al., 2009).

Given the importance of particle collisions for triboelectrification and the need for charge separation to enable electric discharge, the Stokes number (St) is central to understanding our experimental results and for scaling to volcanic eruptions. St describes the degree to which particle velocity is coupled to the gas velocity. Figure 6 shows that the particles smaller than 10 μm used in this study have a St less than about unity, so they are well-coupled

Table 2
Summary of Common Ranges of the Dynamic Variables Relevant for Volcanic Plume Systems and This Study

Variable (unit)	Experiments		Common ranges of the dynamic variables
	Gaudin and Cimarelli (2019)	This study	
Main parameter			
Velocity (m/s)	200–500	200–300	150–500
Particle size (m)	10^{-6}–3×10^{-4}	10^{-6}–3×10^{-4}	10^{-6}–10^{-2}
Vent diameter (m)	2.2×10^{-2}–3.7×10^{-2}	2.8×10^{-2}	100–400
Gas viscosity (Pa s)	2.23×10^{-5}	2.24×10^{-5}	3×10^{-5}
Fluid density (kg/m^3)	1–33	20–108	2–90
Jet dimensionless numbers			
Reynolds number Re	3×10^5–3×10^7	7×10^6–3×10^7	10^7–10^9
Stokes number St	10^{-2}–10^2	10^{-2}–10^2	10^{-4}–10^3
Froude number Fr	3×10^2–10^3	4×10^2–6×10^2	3×10^{-1}–3×10^1

Note. Values were obtained from Carazzo and Jellinek (2012), Burgisser et al. (2005), Roche and Carazzo (2019), and the references therein. The Froude number was determined from Fr = $1/\mathrm{Ri}^{1/2}$ (Roche & Carazzo, 2019).

to the turbulent gas motions, whereas larger particles are not. As in volcanic eruptions, our experiments span the range for St from much less than, to much greater than, unity (Table 2).

For the glass beads, the discharge behavior of the experiments containing a grain size fraction <50 μm (Figures 3a and 3b) shows that the grain size fraction <10 μm is most likely responsible for the observed discharges. The grain size fraction <50 μm includes ~7.3% of grains smaller than 20 μm but only 0.34% smaller than 10 μm, resulting in an almost negligible amount of particles <10 μm in the total particle mixture. A sample mixture containing coarse particles (150–250 μm) and the grain size fraction <50 μm but no particles <10 μm caused no

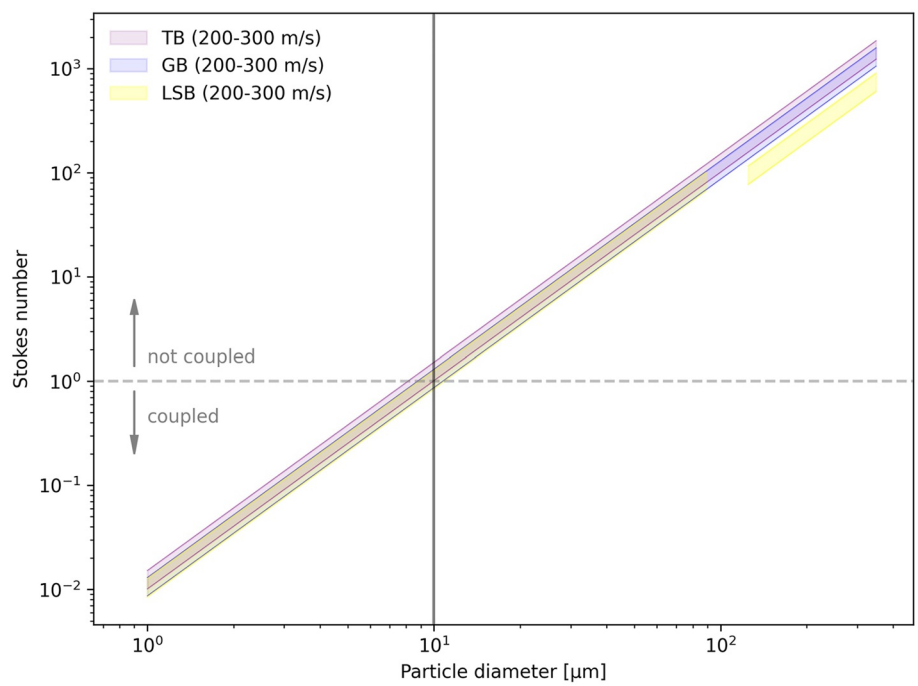

Figure 6. Stokes number (St) as a function of particle diameter for the particles used in this study. The particles are well-coupled to gas motions when St is smaller than 1, which is the case for particles with diameters <10 μm for tholeiitic basalt and soda-lime glass beads. For Laacher See phonolitic pumice, St is calculated with the matrix density for diameters <90 μm and the bulk density for coarse particles >125 μm.

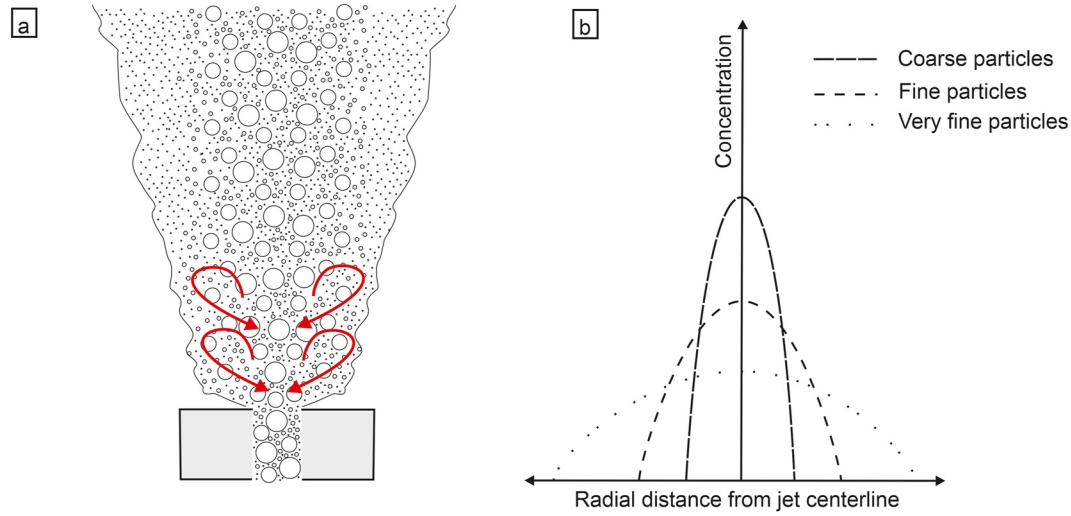

Figure 7. Illustration of particle transport in the jet. The red arrows indicate schematically the turbulent motions generated by shear at the edge of the jet. The very fine particles (St < 1) are coupled to the turbulent gas flow. Depending on their Stokes number, the coarser particles (St > 1) are less coupled to the flow and form a more collimated flow in the middle of the jet. Finer and coarser particles interact with each other by colliding, which charges the particles. The different transport of small and large St particles enables the separation of very fines from larger particles leading to charge separation.

discharges. Although different in chemical composition, TB and GB show similarities in their discharge behavior. TB and GB also have similar St for a given grain size (Figure 6). Figure 3 shows that TB and GB display an increase in the magnitude of discharge with increasing very fine fractions. It appears, however, that there may be a threshold fraction of very fine particles at which the gas-particle mixture becomes electrically saturated and cannot charge/discharge further at the given flow conditions (total mass of particles, particles vs. gas volume, and initial pressure).

The LSB particles have a smaller St number for a given size due to the lower density of the coarse porous fraction. However, the fine fraction of LSB has a density similar to TB and GB, and thus the size of coupled particles is similar to TB and GB. We might therefore expect a somewhat different behavior of the coarse, uncoupled particles in the expanding jet due to their lower density.

The generation of electric discharge requires separation of the charged particles within the jet. The model by Cimarelli et al. (2014) explains why a monodisperse GSD will not cause substantial charging upon rapid decompression as separation of charged particles following different trajectories in the jet is required to generate electrical discharges. Consistent with the predictions of this model, our experiments with solely coarse grain size fractions yielded no discharges.

High-speed camera observations provide information about the gas-particle mixture behavior at the vent. With decreasing grain size and/or decreasing density, the particles are better coupled to the turbulent gas motions, which is visible in the high-speed recordings as a mixed layer surrounding the collimated flow in the middle of the jet. This behavior is illustrated schematically in Figure 7. Charging can occur when particles of different sizes collide in the core of the jet. The entrainment of the small Stokes number particles (very fines) by the turbulence enables the charge separation.

From our experimental results, it appears that for TB and GB, the presence of a very fine fraction is necessary to generate discharges during the experiment. Under the same experimental conditions, LSB does not show significant discharges during decompression despite containing particles <10 μm, whereas grain size mixtures of LSB exhibiting a broader variance in their distribution produce discharges during decompression: The grain size fractions of LSB 90–300 μm differ from the washed grain size fractions 180–250 μm mixed with added amounts of fines in still containing grains sizes in the intermediate range 63–180 μm (Figure 1). Several phenomena might explain the different discharge behavior of LSB. First, very fine particles might adhere to the high internal surface area of the highly vesicular clasts or even get trapped in the pore space of the coarse LSB particles, thereby suppressing separation of particles and their charges. Second, the LSB fraction 90–300 μm contains moderately

fine particles and thus has a broader GSD. Particle collision frequencies are highest for intermediate St, typically between about 1 and 10 (details depend on the type of flow and flow Re), owing to feedback between coupling to turbulent motions and particle concentration in regions with low vorticity (e.g., Sundaram & Collins, 1997; Wang et al., 2000; Zhou et al., 1998). Thus, a broader GSD with more particles having St with order of magnitude from 1 to 10 may enhance the collisions between particles, leading to more charging. The moderately fine particles (63–180 μm) may also provide less internal surface that could trap very fines. Taken together, these dynamics would promote particle charging and separation and, as a result, discharges.

All three samples analyzed in this study are chemically distinct. In addition, they vary texturally: LSB is highly vesicular whereas TB and GB are dense; LSB and TB are irregularly shaped whereas GB particles are mostly spherical. Despite their chemical differences, the TB and GB show similar numbers and intensities in their near-vent discharges (Figure 3), and they also have similar coupling to the gas (Figure 6). For LSB, electric discharge has a different dependence on the GSD; to achieve near-vent discharges, different grain size fractions of LSB have to interact compared to GB and TB. Common to all samples, however, is the need for the presence of very fines to cause discharges. The key characteristic discriminating LSB particles from TB and GB particles is the high vesicularity at moderate and coarse sizes. Based on these observations, acknowledging the small range of compositions and textures we were able to explore, we suggest that textural properties, especially vesicularity, do affect near vent lightning whereas samples' chemistry seems to have a minor influence. We hypothesize that near-vent lightning, is dominated by the motion of particles in response to the transporting gas phase and their interaction with the other particles of the ejected particle mixture, processes that are more affected by textural differences than by chemical differences.

The experimental results and interpretations presented in this study provide some insights into how particle interactions and particle-gas coupling lead to electrical charging and discharge. There are, however, several important limitations, some of which could possibly be addressed in the future with additional experiments and modifications to the experimental methods. First, although the velocity of the particles is a crucial parameter to understand collisions and particle separation, velocities of individual particles could not be determined. The high-speed recordings (up to 50,000 fps) show the motion of the jet, but it was not possible to obtain the speed of individual particles due to the small grain size. Second, although particle clustering is pervasive in flows of solid particles, creating dense regions of concentrated particles surrounded by more dilute regions (Fullmer & Hrenya, 2017), addressing this phenomenon is beyond the scope of our study because we could not image clustering in the jet. Clustering might play a crucial role in the process of particle charging and separation to cause discharges. Third, all experiments in this study were performed at room temperature. Stern et al. (2019) performed shock-tube experiments to investigate the influence of temperature (25°C–320°C) and water content (0–27 wt%) on the charging and discharging behavior of a particle-laden jet. With increasing temperature, they observed a decrease in the jet exit angle, which could result in a higher particle concentration, but only a minor increase in cumulative discharge was observed. They pointed out that an increase in temperature does change the solid and gas properties and therefore the jet dynamics, which could be related to a decrease in net charge at the onset of the discharging activity. Méndez Harper et al. (2020) also investigated the role of humidity and temperature on the charging of particles and observed a decrease in the amount of charge gained by a particle by increasing the temperature. Fourthly, the circularity and the L/D ratio of the samples measure some aspects of particle shape and are similar to each other. Nonetheless, the effect of the surface roughness of the particles was not addressed in this study. As we attribute triboelectrification as the key mechanism to build up charge in the experiments, charging could depend on the roughness of surfaces that interact frictionally and during collisions. Further, particle density, shape, and roughness can affect coupling with the gas. The LSB, for example, has a significantly different mobility in the jet and differs significantly in its discharge behavior. The ability to collide and build up charge depends on the differences in particle motion. The role of Stokes number distributions could be explored more thoroughly. Finally, the experimental apparatus allows the detection of discharges from the jet to the nozzle but not discharges within the jet itself, and thus charge transfer between particles.

5. Conclusion

Shock-tube experiments provide an opportunity to investigate processes in volcanic jets under controlled conditions in the laboratory (Alatorre-Ibargüengoitia et al., 2011; Cigala et al., 2017; Gaudin & Cimarelli, 2019). The presence of very fine to fine particles is observed here to be essential for the production of discharges.

Experiments with a monomodal GSD do not produce any discharges. We thus infer that near-vent lightning may be diagnostic of an ash-rich eruption, especially very fine ash.

Despite their chemical differences, TB and GB produce similar numbers of discharges, supporting the hypothesis that chemical composition does not significantly affect discharge behavior (at least for silicates). A similar conclusion was drawn from charging experiments where particles with different compositions had similar charging rates and charge densities (Méndez Harper & Dufek, 2016) as well as from field observations where VL was observed in different geological settings with varying magma compositions (McNutt & Williams, 2010).

We find that the vesicularity and thus the bulk density of the particles affect the generation of near-vent lightning. Other textural properties, such as shape and surface roughness, also may affect the charging and discharging behavior but require further study. While particle composition does not appear to affect discharging, the vesiculation processes as well as vesicle sizes that affect bulk density are influenced by magma composition. Thus, composition may indirectly affect near-vent lightning by changing clast density. The highly vesiculated LSB, compared to the dense GB and TB, demonstrates this effect.

As noted above, we conclude that the presence of very fine particles (<10 μm) is was required in our experiments to generate discharges during decompression. Particle size and density affect the coupling between gas and particles and therefore their ability to collide with other particles and to follow different trajectories. In our experiments, particles smaller than 10 μm for GB and TB are well-coupled to the gas-phase enabling turbulence in the gas to separate very fines from larger particles after triboelectrification. LSB has a change in density due to the loss of vesicularity with reduced grain size, which affects the coupling of the particles.

VL is increasingly established and recognized as a tool to monitor volcanic eruptions (Cimarelli et al., 2022). Observations from controlled experiments provide insights into the mechanisms that lead to near-vent lightning and, hence, what features of the eruption can be inferred (qualitatively and quantitatively) for VL and thereby inform monitoring strategies. As an example, for a given GSD, electrical discharge is approximately proportional to the mass eruption rate of very fine particles. Equally, the GSD has a major influence on electrical discharge. Thus monitoring near-vent lightning may help constrain in real time some combination of the two key vent parameters, mass eruption rate and GSD (e.g., Beckett et al., 2015; Bonadonna et al., 2012; Dioguardi et al., 2020), that control the height of plumes created by explosive eruptions and the long-distance transport and residence time of very fine ash in the atmosphere. While VL has not traditionally been viewed as a tool for assessing tephra grain size and mass eruption rate (see Table 2 in Bonadonna et al., 2012), our experimental results show that VL is sensitive to both parameters and, hence, holds the potential for real-time monitoring of changing conditions at the vent.

Data Availability Statement

Experimental data are online at the GFZ Data Services (Springsklee et al., 2022). The obtained data were analyzed using the Pandas Data Analysis Library (McKinney, 2010; Reback et al., 2022) and visualized using the Matplotlib Library (Caswell et al., 2021; Hunter, 2007).

Acknowledgments
B.S. and C.S. gratefully acknowledge financial support by the Deutsche Forschungsgemeinschaft (DFG) through the TRR 235 Emergence of Life (Project-ID 364653263). D.B.D. is supported by 2018 ERC ADV Grant 834255 (EAVESDROP). M.M. is supported by the Humboldt Foundation, CIFAR Earth 4D, and NSF 2042173. V.C. acknowledges support through the DFG project CI306/2-1. CC is supported by the DFG project CI 254/2-1 and ERC CON Grant 864052 (VOLTA). Special thanks go to the technical staff of the LMU workshop, especially Markus Sieber. The LSB particles used in the experiments have been generously supplied by ROTEC GmbH (Mühlheim-Kärlich). The authors thank very much the editor and the two anonymous reviewers who provided so many helpful comments and greatly improved the entire manuscript. Open access funding enabled and organized by Projekt DEAL.

References

Aizawa, K., Cimarelli, C., Alatorre-Ibargüengoitia, M. A., Yokoo, A., Dingwell, D. B., & Iguchi, M. (2016). Physical properties of volcanic lightning: Constraints from magnetotelluric and video observations at Sakurajima volcano, Japan. *Earth and Planetary Science Letters*, *444*, 45–55. https://doi.org/10.1016/j.epsl.2016.03.024

Alatorre-Ibargüengoitia, M. A., Scheu, B., & Dingwell, D. B. (2011). Influence of the fragmentation process on the dynamics of Vulcanian eruptions: An experimental approach. *Earth and Planetary Science Letters*, *302*(1–2), 51–59. https://doi.org/10.1016/j.epsl.2010.11.045

Alidibirov, M., & Dingwell, D. B. (1996). An experimental facility for the investigation of magma fragmentation by rapid decompression. *Bulletin of Volcanology*, *58*(5), 411–416. https://doi.org/10.1007/s004450050149

Andrews, B. J., & Manga, M. (2011). Effects of topography on pyroclastic density current runout and formation of coignimbrites. *Geology*, *39*(12), 1099–1102. https://doi.org/10.1130/G32226.1

Andrews, B. J., & Manga, M. (2012). Experimental study of turbulence, sedimentation, and coignimbrite mass partitioning in dilute pyroclastic density currents. *Journal of Volcanology and Geothermal Research*, *225–226*, 30–44. https://doi.org/10.1016/j.jvolgeores.2012.02.011

Arason, P., Bennett, A. J., & Burgin, L. E. (2011). Charge mechanism of volcanic lightning revealed during the 2010 eruption of Eyjafjallajökull. *Journal of Geophysical Research*, *116*, B00C03. https://doi.org/10.1029/2011JB008651

Ayris, P. M., & Delmelle, P. (2012). The immediate environmental effects of tephra emission. *Bulletin of Volcanology*, *74*(9), 1905–1936. https://doi.org/10.1007/s00445-012-0654-5

Beckett, F. M., Witham, C. S., Hort, M. C., Stevenson, J. A., Bonadonna, C., & Millington, S. C. (2015). Sensitivity of dispersion model forecasts of volcanic ash clouds to the physical characteristics of the particles. *Journal of Geophysical Research: Atmospheres*, *120*(22), 11636–11652. https://doi.org/10.1002/2015JD023609

Behnke, S. A., Edens, H. E., Thomas, R. J., Smith, C. M., McNutt, S. R., Van Eaton, A. R., et al. (2018). Investigating the origin of continual radio frequency impulses during explosive volcanic eruptions. *Journal of Geophysical Research: Atmospheres*, *123*(8), 4157–4174. https://doi.org/10.1002/2017JD027990

Behnke, S. A., Thomas, R. J., McNutt, S. R., Schneider, D. J., Krehbiel, P. R., Rison, W., & Edens, H. E. (2013). Observations of volcanic lightning during the 2009 eruption of Redoubt Volcano. *Journal of Volcanology and Geothermal Research*, *259*, 214–234. https://doi.org/10.1016/j.jvolgeores.2011.12.010

Bennett, A. J., Odams, P., Edwards, D., & Arason, Þ. (2010). Monitoring of lightning from the April–May 2010 Eyjafjallajökull volcanic eruption using a very low frequency lightning location network. *Environmental Research Letters*, *5*(4), 044013. https://doi.org/10.1088/1748-9326/5/4/044013

Björnsson, S., Blanchard, D. C., & Spencer, A. T. (1967). Charge generation due to contact of saline waters with molten lava. *Journal of Geophysical Research*, *72*(4), 1311–1323. https://doi.org/10.1029/JZ072i004p01311

Bonadonna, C., Folch, A., Loughlin, S., & Puempel, H. (2012). Future developments in modelling and monitoring of volcanic ash clouds: Outcomes from the first IAVCEI-WMO workshop on Ash Dispersal Forecast and Civil Aviation. *Bulletin of Volcanology*, *74*, 1–10. https://doi.org/10.1007/s00445-011-0508-6

Burgisser, A., Bergantz, G. W., & Breidenthal, R. E. (2005). Addressing complexity in laboratory experiments: The scaling of dilute multiphase flows in magmatic systems. *Journal of Volcanology and Geothermal Research*, *141*(3–4), 245–265. https://doi.org/10.1016/j.jvolgeores.2004.11.001

Carazzo, G., & Jellinek, A. M. (2012). A new view of the dynamics, stability and longevity of volcanic clouds. *Earth and Planetary Science Letters*, *325–326*, 39–51. https://doi.org/10.1016/j.epsl.2012.01.025

Caswell, T. A., Droettboom, M., Lee, A., Sales de Andrade, E., Hoffmann, T., Hunter, J., et al. (2021). matplotlib/matplotlib: REL: v3.5.1 [Dataset]. Zenodo. https://doi.org/10.5281/zenodo.5773480

Cigala, V., Kueppers, U., Peña Fernández, J. J., Taddeucci, J., Sesterhenn, J., & Dingwell, D. B. (2017). The dynamics of volcanic jets: Temporal evolution of particles exit velocity from shock-tube experiments. *Journal of Geophysical Research: Solid Earth*, *122*(8), 6031–6045. https://doi.org/10.1002/2017JB014149

Cimarelli, C., Alatorre-Ibargüengoitia, M. A., Aizawa, K., Yokoo, A., Díaz-Marina, A., Iguchi, M., & Dingwell, D. B. (2016). Multiparametric observation of volcanic lightning: Sakurajima Volcano, Japan. *Geophysical Research Letters*, *43*(9), 4221–4228. https://doi.org/10.1002/2015GL067445

Cimarelli, C., Alatorre-Ibargüengoitia, M. A., Kueppers, U., Scheu, B., & Dingwell, D. B. (2014). Experimental generation of volcanic lightning. *Geology*, *42*(1), 79–82. https://doi.org/10.1130/G34802.1

Cimarelli, C., Behnke, S., Genareau, K., Méndez Harper, J., & Van Eaton, A. R. (2022). Volcanic electrification: Recent advances and future perspectives. *Bulletin of Volcanology*, *84*(8), 78. https://doi.org/10.1007/s00445-022-01591-3

Cimarelli, C., Costa, A., Mueller, S., & Mader, H. M. (2011). Rheology of magmas with bimodal crystal size and shape distributions: Insights from analog experiments. *Geochemistry, Geophysics, Geosystems*, *12*(7), Q07024. https://doi.org/10.1029/2011GC003606

Cimarelli, C., & Genareau, K. (2022). A review of volcanic electrification of the atmosphere and volcanic lightning. *Journal of Volcanology and Geothermal Research*, *422*, 107449. https://doi.org/10.1016/j.jvolgeores.2021.107449

Dioguardi, F., Beckett, F., Dürig, T., & Stevenson, J. A. (2020). The impact of eruption source parameter uncertainties on ash dispersion forecasts during explosive volcanic eruptions. *Journal of Geophysical Research: Atmospheres*, *125*(17), e2020JD032717. https://doi.org/10.1029/2020JD032717

Douillet, G. A., Rasmussen, K. R., Kueppers, U., Castro, D. L., Merrison, J. P., Iversen, J. J., & Dingwell, D. B. (2014). Saltation threshold for pyroclasts at various bedslopes: Wind tunnel measurements. *Journal of Volcanology and Geothermal Research*, *278–279*, 14–24. https://doi.org/10.1016/j.jvolgeores.2014.03.011

Forward, K. M., Lacks, D. J., & Sankaran, R. M. (2009a). Charge segregation depends on particle size in triboelectrically charged granular materials. *Physical Review Letters*, *102*(2), 028001. https://doi.org/10.1103/PhysRevLett.102.028001

Forward, K. M., Lacks, D. J., & Sankaran, R. M. (2009b). Methodology for studying particle–particle triboelectrification in granular materials. *Journal of Electrostatics*, *67*(2–3), 178–183. https://doi.org/10.1016/j.elstat.2008.12.002

Fullmer, W. D., & Hrenya, C. M. (2017). The clustering instability in rapid granular and gas-solid flows. *Annual Review of Fluid Mechanics*, *49*(1), 485–510. https://doi.org/10.1146/annurev-fluid-010816-060028

Gaudin, D., & Cimarelli, C. (2019). The electrification of volcanic jets and controlling parameters: A laboratory study. *Earth and Planetary Science Letters*, *513*, 69–80. https://doi.org/10.1016/j.epsl.2019.02.024

Hargie, K. A., Van Eaton, A. R., Mastin, L. G., Holzworth, R. H., Ewert, J. W., & Pavolonis, M. (2019). Globally detected volcanic lightning and umbrella dynamics during the 2014 eruption of Kelud, Indonesia. *Journal of Volcanology and Geothermal Research*, *382*, 81–91. https://doi.org/10.1016/j.jvolgeores.2018.10.016

Hunter, J. D. (2007). Matplotlib: A 2D graphics environment. *Computing in Science & Engineering*, *9*(3), 90–95. https://doi.org/10.1109/MCSE.2007.55

James, M. R., Lane, S. J., & Gilbert, J. S. (2000). Volcanic plume electrification: Experimental investigation of a fracture-charging mechanism. *Journal of Geophysical Research*, *105*(B7), 16641–16649. https://doi.org/10.1029/2000JB900068

Jessop, D. E., & Jellinek, A. M. (2014). Effects of particle mixtures and nozzle geometry on entrainment into volcanic jets. *Geophysical Research Letters*, *41*(11), 3858–3863. https://doi.org/10.1002/2014GL060059

Kikuchi, K., & Endoh, T. (1982). Atmospheric electrical properties of volcanic ash particles in the eruption of Mt. Usu volcano, 1977. *Journal of the Meteorological Society of Japan. Ser. II*, *60*(1), 548–561. https://doi.org/10.2151/jmsj1965.60.1_548

McKinney, W. (2010). Data structures for statistical computing in python. In S. Van der Walt & J. Millman (Eds.), *Proceedings of the 9th Python in Science Conference* (pp. 56–61). https://doi.org/10.25080/Majora-92bf1922-00a

McNutt, S. R., & Williams, E. R. (2010). Volcanic lightning: Global observations and constraints on source mechanisms. *Bulletin of Volcanology*, *72*(10), 1153–1167. https://doi.org/10.1007/s00445-010-0393-4

Méndez Harper, J., Cimarelli, C., Cigala, V., Kueppers, U., & Dufek, J. (2021). Charge injection into the atmosphere by explosive volcanic eruptions through triboelectrification and fragmentation charging. *Earth and Planetary Science Letters*, *574*, 117162. https://doi.org/10.1016/j.epsl.2021.117162

Méndez Harper, J., Courtland, L., Dufek, J., & McAdams, J. (2020). Microphysical effects of water content and temperature on the triboelectrification of volcanic ash on long time scales. *Journal of Geophysical Research: Atmospheres*, *125*(14), e2019JD031498. https://doi.org/10.1029/2019JD031498

Méndez Harper, J., & Dufek, J. (2016). The effects of dynamics on the triboelectrification of volcanic ash. *Journal of Geophysical Research: Atmospheres*, *121*(14), 8209–8228. https://doi.org/10.1002/2015JD024275

Mueller, S. P., Helo, C., Keller, F., Taddeucci, J., & Castro, J. M. (2018). First experimental observations on melting and chemical modification of volcanic ash during lightning interaction. *Scientific Reports*, *8*(1), 1389. https://doi.org/10.1038/s41598-018-19608-3

Nicoll, K., Airey, M., Cimarelli, C., Bennett, A., Harrison, G., Gaudin, D., et al. (2019). First in situ observations of gaseous volcanic plume electrification. *Geophysical Research Letters*, *46*(6), 3532–3539. https://doi.org/10.1029/2019GL082211

Paola, C., Straub, K., Mohrig, D., & Reinhardt, L. (2009). The "unreasonable effectiveness" of stratigraphic and geomorphic experiments. *Earth-Science Reviews*, *97*(1–4), 1–43. https://doi.org/10.1016/j.earscirev.2009.05.003

Prata, A. T., Folch, A., Prata, A. J., Biondi, R., Brenot, H., Cimarelli, C., et al. (2020). Anak Krakatau triggers volcanic freezer in the upper troposphere. *Scientific Reports*, *10*(1), 3584. https://doi.org/10.1038/s41598-020-60465-w

Rayborn, L., & Jellinek, A. M. (2022). Random forest predictions of fine ash concentration and charging processes from experimentally generated volcanic discharges. *Journal of Geophysical Research: Solid Earth*, *127*(5), e2021JB023599. https://doi.org/10.1029/2021JB023599

Reback, J., jbrockmendel, McKinney, W., Van den Bossche, J., Augspurger, T., Roeschke, M., Hawkins, S., et al. (2022). pandas-dev/pandas: Pandas 1.4.2 [Dataset]. Zenodo. https://doi.org/10.5281/zenodo.6408044

Roche, O. (2012). Depositional processes and gas pore pressure in pyroclastic flows: An experimental perspective. *Bulletin of Volcanology*, *74*(8), 1807–1820. https://doi.org/10.1007/s00445-012-0639-4

Roche, O., & Carazzo, G. (2019). The contribution of experimental volcanology to the study of the physics of eruptive processes, and related scaling issues: A review. *Journal of Volcanology and Geothermal Research*, *384*, 103–150. https://doi.org/10.1016/j.jvolgeores.2019.07.011

Scheu, B., & Dingwell, D. B. (2022). Magma fragmentation. *Reviews in Mineralogy and Geochemistry*, *87*(1), 767–800. https://doi.org/10.2138/rmg.2021.87.16

Springsklee, C., Scheu, B., Manga, M., Cigala, V., Cimarelli, C., & Dingwell, D. B. (2022). *Experimental dataset for the influence of grain size distribution on experimental volcanic lightning*. GFZ Data Services. https://doi.org/10.5880/fidgeo.2022.009

Stern, S., Cimarelli, C., Gaudin, D., Scheu, B., & Dingwell, D. B. (2019). Electrification of experimental volcanic jets with varying water content and temperature. *Geophysical Research Letters*, *46*(20), 11136–11145. https://doi.org/10.1029/2019GL084678

Sundaram, S., & Collins, L. R. (1997). Collision statistics in an isotropic particle-laden turbulent suspension. Part 1. Direct numerical simulations. *Journal of Fluid Mechanics*, *335*, 75–109. https://doi.org/10.1017/S0022112096004454

Thomas, R. J., McNutt, S. R., Krehbiel, P. R., Rison, W., Aulich, G., Edens, H. E., et al. (2010). Lightning and electrical activity during the 2006 eruption of Augustine Volcano, chapter 25. In J. A. Power, M. L. Coombs, & J. T. Freymueller (Eds.), *The 2006 eruption of Augustine Volcano, Alaska* (Vol. 1769. pp. 579–608). US Geological Survey Professional Paper. Retrieved from https://pubs.usgs.gov/pp/1769/chapters/p1769_chapter25.pdf

Van Eaton, A. R., Amigo, Á., Bertin, D., Mastin, L. G., Giacosa, R. E., González, J., et al. (2016). Volcanic lightning and plume behavior reveal evolving hazards during the April 2015 eruption of Calbuco volcano, Chile. *Geophysical Research Letters*, *43*(7), 3563–3571. https://doi.org/10.1002/2016GL068076

Van Eaton, A. R., Schneider, D. J., Smith, C. M., Haney, M. M., Lyons, J. J., Said, R., et al. (2020). Did ice-charging generate volcanic lightning during the 2016–2017 eruption of Bogoslof volcano, Alaska? *Bulletin of Volcanology*, *82*(3), 24. https://doi.org/10.1007/s00445-019-1350-5

Vossen, C. E. J., Cimarelli, C., Bennett, A. J., Geisler, A., Gaudin, D., Miki, D., et al. (2021). Long-term observation of electrical discharges during persistent Vulcanian activity. *Earth and Planetary Science Letters*, *570*, 117084. https://doi.org/10.1016/j.epsl.2021.117084

Vossen, C. E. J., Cimarelli, C., Bennett, A. J., Schmid, M., Kueppers, U., Ricci, T., & Taddeucci, J. (2022). The electrical signature of mafic explosive eruptions at Stromboli volcano, Italy. *Scientific Reports*, *12*(1), 9049. https://doi.org/10.1038/s41598-022-12906-x

Wang, L.-P., Wexler, A. S., & Zhou, Y. (2000). Statistical mechanical description and modelling of turbulent collision of inertial particles. *Journal of Fluid Mechanics*, *415*, 117–153. https://doi.org/10.1017/S0022112000008661

Weit, A., Roche, O., Dubois, T., & Manga, M. (2018). Experimental measurement of the solid particle concentration in geophysical turbulent gas-particle mixtures. *Journal of Geophysical Research: Solid Earth*, *123*(5), 3747–3761. https://doi.org/10.1029/2018JB015530

Weit, A., Roche, O., Dubois, T., & Manga, M. (2019). Maximum solid phase concentration in geophysical turbulent gas-particle flows: Insights from laboratory experiments. *Geophysical Research Letters*, *46*(12), 6388–6396. https://doi.org/10.1029/2019GL082658

Yuen, D. A., Scruggs, M. A., Spera, F. J., Zheng, Y., Hu, H., McNutt, S. R., et al. (2022). Under the surface: Pressure-induced planetary-scale waves, volcanic lightning, and gaseous clouds caused by the submarine eruption of Hunga Tonga-Hunga Ha'apai volcano. *Earthquake Research Advances*, *2*(3), 100134. https://doi.org/10.1016/j.eqrea.2022.100134

Zhou, Y., Wexler, A. S., & Wang, L.-P. (1998). On the collision rate of small particles in isotropic turbulence. II. Finite inertia case. *Physics of Fluids*, *10*(5), 1206–1216. https://doi.org/10.1063/1.869644